



<http://www.diva-portal.org>

## Postprint

This is the accepted version of a paper published in *Optics Express*. This paper has been peer-reviewed but does not include the final publisher proof-corrections or journal pagination.

Citation for the original published paper (version of record):

Calil Kores, C., Ismail, N., Geskus, D., Dijkstra, M., Bernhardt, E. et al. (2018)  
Temperature dependence of the spectral characteristics of distributed-feedback  
resonators  
*Optics Express*, 26(4): 4892-4905

Access to the published version may require subscription.

N.B. When citing this work, cite the original published paper.

Permanent link to this version:

<http://urn.kb.se/resolve?urn=urn:nbn:se:kth:diva-224792>



# Temperature dependence of the spectral characteristics of distributed-feedback resonators

CRISTINE CALIL KORES,<sup>1,2</sup> NUR ISMAIL,<sup>1</sup> DIMITRI GESKUS,<sup>1</sup> MEINDERT DIJKSTRA,<sup>3</sup> EDWARD H. BERNHARDI,<sup>1,4</sup> AND MARKUS POLLNAU<sup>1,5,\*</sup>

<sup>1</sup>Department of Materials and Nano Physics, School of Information and Communication Technology, KTH – Royal Institute of Technology, Electrum 229, Isafjordsgatan 22–24, 16440 Kista, Sweden

<sup>2</sup>Department of Applied Physics, School of Engineering Sciences, Roslagstullsbacken 21, 10691 Stockholm, Sweden

<sup>3</sup>Optical Sciences, MESA + Institute, University of Twente, P.O. Box 217, 7500 AE Enschede, The Netherlands

<sup>4</sup>Visiting scientist

<sup>5</sup>Advanced Technology Institute, Department of Electrical and Electronic Engineering, University of Surrey, Guildford GU2 7XH, UK

\*[m.pollnau@surrey.ac.uk](mailto:m.pollnau@surrey.ac.uk)

**Abstract:** We characterize the spectral response of a distributed-feedback resonator when subject to a thermal chirp. An Al<sub>2</sub>O<sub>3</sub> rib waveguide with a corrugated surface Bragg grating inscribed into its SiO<sub>2</sub> top cladding is experimentally investigated. We induce a near-to-linear temperature gradient along the resonator, leading to a similar variation of the grating period, and characterize its spectral response in terms of wavelength and linewidth of the resonance peak. Simulations are carried out, showing good agreement with the experimental results and indicating that the wavelength of the resonance peak is a result only of the total accumulated phase shift. For any chirp profile we are able to calculate the reflectivities at the resonance wavelength, and this information largely explains how the linewidth of the resonance changes. This result shows that the increase in linewidth is governed by the increase of the resonator outcoupling losses.

© 2018 Optical Society of America under the terms of the [OSA Open Access Publishing Agreement](#)

**OCIS codes:** (140.4780) Optical resonators; (140.3410) Laser resonators; (140.3490) Lasers, distributed-feedback; (230.1480) Bragg reflectors; (050.1590) Chirping.

## References and links

1. H. G. Limberger, D. M. Costantini, R. P. Salathé, C. A. P. Muller, G. R. Fox, and N. H. Ky, “Efficient miniature fiber optic tunable filter based on intra-core Bragg grating and electrically resistive coating,” *IEEE Photonics Technol. Lett.* **10**(3), 361–363 (1998).
2. D. M. Costantini, C. A. P. Muller, S. A. Vasiliev, H. G. Limberger, and R. P. Salathé, “Tunable loss filter based on metal coated long period fiber grating,” *IEEE Photonics Technol. Lett.* **11**(11), 1458–1460 (1999).
3. G. Meltz, J. R. Dunphy, W. H. Glenn, J. D. Farina, and F. J. Leonberger, “Fiber optic temperature and strain sensors,” *Proc. SPIE* **798**, 104–114 (1987).
4. M. L. Dakss, L. Kuhn, P. F. Heidrich, and B. A. Scott, “Grating coupler for efficient excitation of optical guided waves in thin films,” *Appl. Phys. Lett.* **16**(12), 523–525 (1970).
5. H. Kogelnik and C. V. Shank, “Coupled-wave theory of distributed feedback lasers,” *J. Appl. Phys.* **43**(5), 2327–2335 (1972).
6. T.-Y. Chung, A. Rapaport, V. Smirnov, L. B. Glebov, M. C. Richardson, and M. Bass, “Solid-state laser spectral narrowing using a volumetric photothermal refractive Bragg grating cavity mirror,” *Opt. Lett.* **31**(2), 229–231 (2006).
7. G. A. Ball, W. W. Morey, and W. H. Glenn, “Standing-wave monomode erbium fiber laser,” *IEEE Photonics Technol. Lett.* **3**(7), 613–615 (1991).
8. S. Blaize, L. Bastard, C. Cassagnetes, and J. E. Broquin, “Multiwavelengths DFB waveguide laser arrays in Yb-Er codoped phosphate glass substrate,” *IEEE Photonics Technol. Lett.* **15**(4), 516–518 (2003).
9. E. H. Bernhardt, H. A. G. M. van Wolferen, L. Agazzi, M. R. H. Khan, C. G. H. Roeloffzen, K. Wörhoff, M. Pollnau, and R. M. de Ridder, “Ultra-narrow-linewidth, single-frequency distributed feedback waveguide laser in Al<sub>2</sub>O<sub>3</sub>:Er<sup>3+</sup> on silicon,” *Opt. Lett.* **35**(14), 2394–2396 (2010).

10. E. H. Bernhardt, Q. Lu, H. A. G. M. van Wolferen, K. Wörhoff, R. M. de Ridder, and M. Pollnau, "Monolithic distributed Bragg reflector cavities in  $\text{Al}_2\text{O}_3$  with quality factors exceeding  $10^6$ ," *Photon. Nanostructures* **9**(3), 225–234 (2011).
11. A. Suzuki and K. Tada, "Theory and experiment on distributed feedback lasers with chirped grating," *Proc. SPIE* **0239**, 10–18 (1981).
12. P. Zhou and G. S. Lee, "Mode selection and spatial hole burning suppression of a chirped grating distributed feedback laser," *Appl. Phys. Lett.* **56**(15), 1400–1402 (1990).
13. S. Hansmann, H. Burkhard, H. Hillmer, and A. Grabmeier, "Continuously distributed phase shifts in chirped DFB lasers using bent waveguides," *Electron. Lett.* **30**(18), 1483–1484 (1994).
14. Y. A. C. Livanos, A. Katzir, and A. Yariv, "Fabrication of grating structures with variable period," *Opt. Commun.* **20**(1), 179–182 (1977).
15. A. Katzir, A. Livanos, J. Shellan, and A. Yariv, "Chirped gratings in integrated optics," *IEEE J. Quantum Electron.* **13**(4), 296–304 (1977).
16. N. Chen, Y. Nakano, K. Okamoto, K. Tada, G. I. Morthier, and R. G. Baets, "Analysis, fabrication, and characterization of tunable DFB lasers with chirped gratings," *IEEE J. Sel. Top. Quantum Electron.* **3**(2), 541–546 (1997).
17. G. P. Agrawal, J. E. Geusic, and P. J. Anthony, "Distributed feedback lasers with multiple phase-shift regions," *Appl. Phys. Lett.* **53**(3), 178–179 (1988).
18. P. Zhou and G. S. Lee, "Chirped grating  $\lambda/4$  shifted distributed feedback laser with uniform longitudinal field distribution," *Electron. Lett.* **26**(20), 1660–1661 (1990).
19. M. Okai, T. Tsuchiya, K. Uomi, N. Chinone, and T. Harada, "Corrugation-pitch modulated MQW-DFB lasers with narrow spectral linewidth," *IEEE J. Quantum Electron.* **27**(6), 1767–1772 (1991).
20. J. Lauzon, S. Thibault, J. Martin, and F. Ouellette, "Implementation and characterization of fiber Bragg gratings linearly chirped by a temperature gradient," *Opt. Lett.* **19**(23), 2027–2029 (1994).
21. J. A. Rogers, B. J. Eggleton, R. J. Jackman, G. R. Kowach, and T. A. Strasser, "Dual on-fiber thin-film heaters for fiber gratings with independently adjustable chirp and wavelength," *Opt. Lett.* **24**(19), 1328–1330 (1999).
22. N. Q. Ngo, D. Liu, S. C. Tjin, X. Dong, and P. Shum, "Thermally switchable and discretely tunable comb filter with a linearly chirped fiber Bragg grating," *Opt. Lett.* **30**(22), 2994–2996 (2005).
23. Y. T. Dai and J. P. Yao, "Numerical study of a DFB semiconductor laser and laser array with chirped structure based on the equivalent chirp technology," *IEEE J. Quantum Electron.* **44**(10), 938–945 (2008).
24. G. D. Marshall, R. J. Williams, N. Jovanovic, M. J. Steel, and M. J. Withford, "Point-by-point written fiber-Bragg gratings and their application in complex grating designs," *Opt. Express* **18**(19), 19844–19859 (2010).
25. G. A. Miller, J. R. Peele, C. G. Askins, and G. A. Cranch, "Characterization of strong fiber Bragg gratings using an applied thermal chirp and iterative algorithm," *Appl. Opt.* **50**(36), 6617–6626 (2011).
26. S. Tjörnhammar, B. Jacobsson, V. Pasiskevicius, and F. Laurell, "Thermal limitations of volume Bragg gratings used in lasers for spectral control," *J. Opt. Soc. Am. B* **30**(6), 1402–1409 (2013).
27. M. Born and E. Wolf, *Principles of Optics* (Pergamon, 1975), Chap. 1.
28. K. Wörhoff, J. D. B. Bradley, F. Ay, D. Geskus, T. P. Blauwendraat, and M. Pollnau, "Reliable low-cost fabrication of low-loss  $\text{Al}_2\text{O}_3\text{:Er}^{3+}$  waveguides with 5.4-dB optical gain," *IEEE J. Quantum Electron.* **45**(5), 454–461 (2009).
29. J. D. B. Bradley, F. Ay, K. Wörhoff, and M. Pollnau, "Fabrication of low-loss channel waveguides in  $\text{Al}_2\text{O}_3$  and  $\text{Y}_2\text{O}_3$  layers by inductively coupled plasma reactive ion etching," *Appl. Phys. B* **89**(2–3), 311–318 (2007).
30. E. H. Bernhardt, H. A. G. M. van Wolferen, K. Wörhoff, R. M. de Ridder, and M. Pollnau, "Highly efficient, low-threshold monolithic distributed-Bragg-reflector channel waveguide laser in  $\text{Al}_2\text{O}_3\text{:Yb}^{3+}$ ," *Opt. Lett.* **36**(5), 603–605 (2011).
31. K. Tada, Y. Nakano, and A. Ushirokawa, "Proposal of a distributed feedback laser with nonuniform stripe width for complete single-mode oscillation," *Electron. Lett.* **20**(2), 82–84 (1984).
32. M. Usami, S. Akiba, and K. Utaka, "Asymmetric  $\lambda/4$ -shifted InGaAsP/InP DFB lasers," *IEEE J. Quantum Electron.* **23**(6), 815–821 (1987).
33. H. Soda and H. Imai, "Analysis of the spectrum behavior below the threshold in DFB lasers," *IEEE J. Quantum Electron.* **22**(5), 637–641 (1986).
34. N. Ismail, C. C. Kores, D. Geskus, and M. Pollnau, "Fabry-Pérot resonator: spectral line shapes, generic and related Airy distributions, linewidths, finesse, and performance at low or frequency-dependent reflectivity," *Opt. Express* **24**(15), 16366–16389 (2016).
35. M. Eichhorn, S. T. Friedrich-Thornton, E. Heumann, and G. Huber, "Spectroscopic properties of  $\text{Er}^{3+}$ :YAG at 300–550 K and their effects on the 1.6  $\mu\text{m}$  laser transition," *Appl. Phys. B* **91**(2), 249–256 (2008).
36. Y. S. Yong, S. Aravazhi, S. A. Vázquez-Córdova, J. J. Carjaval, F. Diaz, J. L. Herek, S. M. García-Blanco, and M. Pollnau, "Temperature-dependent absorption and emission of potassium double tungstates with high ytterbium content," *Opt. Express* **24**(23), 26825–26837 (2016).
37. C. J. Wu, B. H. Chu, and M. T. Weng, "Analysis of optical reflection in a chirped distributed Bragg reflector," *J. Electromagn. Waves Appl.* **23**(1), 129–138 (2009).
38. J. Hong, W. Huang, and T. Makino, "On the transfer matrix method for distributed-feedback waveguide devices," *J. Lightwave Technol.* **10**(12), 1860–1868 (1992).
39. T. Makino, "Transfer matrix method with applications to distributed feedback optical devices," *Prog. Electromagn. Res.* **10**, 271–319 (1995).

40. G. Björk and O. Nilsson, "A new exact and efficient numerical matrix theory of complicated laser structures: properties of asymmetric phase-shifted DFB lasers," *J. Lightwave Technol.* **5**(1), 140–146 (1987).
41. A. Yariv, "Coupled-mode theory for guided-wave optics," *IEEE J. Quantum Electron.* **9**(9), 919–933 (1973).
42. Purnawirman, N. Li, E. S. Magden, G. Singh, M. Moresco, T. N. Adam, G. Leake, D. Coolbaugh, J. D. B. Bradley, and M. R. Watts, "Wavelength division multiplexed light source monolithically integrated on a silicon photonics platform," *Opt. Lett.* **42**(9), 1772–1775 (2017).
43. M. Pollnau, P. J. Hardman, M. A. Kern, W. A. Clarkson, and D. C. Hanna, "Upconversion-induced heat generation and thermal lensing in Nd:YLF and Nd:YAG," *Phys. Rev. B* **58**(24), 16076–16092 (1998).
44. M. R. Saleem, R. Ali, S. Honkanen, and J. Turunen, "Thermal properties of thin Al<sub>2</sub>O<sub>3</sub> films and their barrier layer effect on thermo-optic properties of TiO<sub>2</sub> films grown by atomic layer deposition," *Thin Solid Films* **542**, 257–262 (2013).
45. L. Agazzi, "Spectroscopic excitation and quenching processes in rare-earth-ion-doped Al<sub>2</sub>O<sub>3</sub> and their impact on amplifier and laser performance," Ph.D. thesis, University of Twente, The Netherlands (2012).

## 1. Introduction

Periodic corrugated structures have been extensively investigated over the last decades, for their significant and wide range of applications, being employed as spectral filters [1,2], temperature and strain sensors [3], couplers [4], beam splitters, as well as part of the resonant structure in distributed-feedback (DFB) [5] and distributed-Bragg-reflector (DBR) lasers. The latter application relies on the fact that the Bragg grating provides very high wavelength selectivity [6], hence allowing for the development of ultranarrow-linewidth lasers [7–10]. The grating period has a strong influence on the longitudinal-mode selectivity [11–13]. Gratings with non-uniform period (chirped gratings) have received much interest [14–16], and substantial attention has been paid to the design of chirped gratings that manipulate the intracavity power distribution and avoid spatial hole burning in DFB lasers [17–19].

Despite careful design of DFB resonators for ultranarrow-linewidth laser operation, asymmetric heating of the device due to non-uniformly absorbed pump power in optically pumped lasers, which is partially converted into heat, may cause an undesired chirp in the Bragg structure. The resulting changes in refractive index as well as material expansion influence the resonance frequency and linewidth of the central emission line. Thermally induced chirped gratings are reported in the literature under the scope of power stability and spectral response [20–26], however, to the best of our knowledge, a complete and satisfactory explanation of the relationship between the chirped grating profile and the linewidth produced by the resonator is still lacking.

In this work, we investigate the spectral characteristics of DFB resonators with a thermally induced chirp in their Bragg grating. A temperature gradient with an approximately linear profile is experimentally produced along the waveguide resonator, and the wavelength of the resonance peak and its linewidth are characterized. The experimental results show good agreement with simulations based on Born and Wolf's [27] characteristic-matrix approach.

## 2. Experimental

### 2.1 Laser resonator under investigation

The sample investigated in this work is an amorphous Al<sub>2</sub>O<sub>3</sub>:Yb<sup>3+</sup> rib waveguide with an Yb<sup>3+</sup> concentration of  $4.37 \times 10^{20} \text{ cm}^{-3}$ , deposited by RF reactive co-sputtering from metallic Al and Yb targets onto a thermally oxidized silicon wafer [28] and subsequently micro-structured by chlorine-based reactive ion etching [29], with a SiO<sub>2</sub> top cladding of 350 nm thickness added. The rib waveguide has a length of  $\ell = 1 \text{ cm}$  and  $2.5 \times 1.0 \mu\text{m}^2$  lateral cross section, designed to support only fundamental-transverse-mode propagation [Fig. 1(a)]. A corrugated homogeneous Bragg grating, where  $\kappa = 8.33 \text{ cm}^{-1}$  is the grating coupling coefficient per unit length [10], is inscribed into the SiO<sub>2</sub> top cladding by laser interference lithography and subsequent reactive ion etching [9,10], providing the necessary feedback for single-longitudinal-mode laser operation at the Bragg wavelength  $\lambda_B$  [30].

The  $\lambda_B/4$  phase shift required for producing a resonance within the reflection band of the Bragg grating is achieved by an adiabatic tapering of the waveguide structure [31,9], in which

the waveguide width first increases and then decreases gradually according to a  $\sin^2$  function from 2.5 to 2.85  $\mu\text{m}$  over a total length of 2 mm. As a consequence, the effective refractive index to which the propagating mode is subject also increases with the same function. The tapered section of the waveguide is designed to result in an accumulated phase shift of  $\lambda_B/4$ . The phase-shift region is centered at the position  $z_{ps} = 7$  mm in order to yield higher output powers in one direction [32,9]. Having introduced the tapering of the waveguide, the resultant modulation of the refractive index is no longer periodic, and therefore the Bragg grating becomes non-periodic.

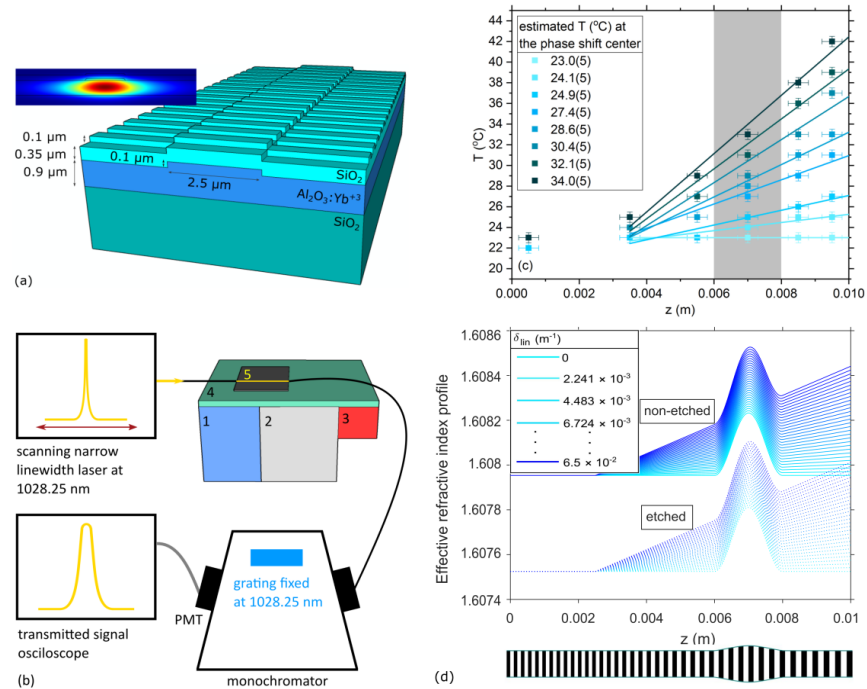


Fig. 1. (a) Illustration of DFB rib waveguide. Inset: transverse profile of guided fundamental mode. (b) Schematic of experimental setup for inducing a temperature gradient and measuring wavelength and linewidth of the resonance peak. 1: block with circulating water at room temperature (22°C); 2: ~15 mm long aluminum block; 3: metal block with power resistor connected to a control-loop feedback mechanism for controlled temperature increase; 4: thermally conductive layer, consisting of thermal paste; 5: sample, where the DFB resonator is indicated by a yellow line. (c) Measured temperature (squares) along the waveguide and fit (lines) by a linear function. (d) Modulation of effective refractive index along the propagation direction, as a combined result of the increase in waveguide width to achieve a  $\lambda/4$  phase shift and the considered values for the linear chirp. The “non-etched” and “etched” series of graphs represent the half period of the non-etched and etched grating, respectively. The waveguide with a linear chirp profile is represented at the bottom of the figure.

## 2.2 Generation of temperature gradient

Besides the capability of homogeneously heating the entire sample, we generate experimentally a temperature gradient by controlling the temperature in the sample holder onto which the sample is mounted, along the waveguide direction. The sample holder [Fig. 1(b)] consists of a cooled metal block, an aluminum block, and a heated metal block. A layer of thermally conductive material is added, onto which the sample is mounted to ensure adequate heat transfer between the holder and the sample.

For the set of heating temperatures used in the experiment, the temperature on the top surface of the sample holder is measured using a thermocouple sensor with a temperature

accuracy of  $\pm 0.5$  K, in several positions along the surface where the waveguide is to be placed [Fig. 1(c)]. As a simplification for the thermal modeling, we consider that air cooling is approximately the same for the sample holder and for the sample when it is mounted onto it. The temperature along the waveguide is fitted by a linear function beginning with the data points at  $z_0 = 3.5$  mm, from which the temperature at the center of the phase shift is estimated.

### 2.3 Resonance measurement

The approximately Lorentzian-shaped resonance near 1028.25 nm is measured in the unpumped sample, hence including the full absorption loss by the Yb ions, and the peak wavelength and full-width-at-half-maximum (FWHM) linewidth of the resonance are characterized. Investigations of the unpumped sample provide insightful information about the behavior of light inside the optical resonator [33], being of crucial importance for understanding the behavior of the resonator during laser operation.

As a probe beam, the signal from a scanning narrow-linewidth laser (DLC DL pro, TOPTICA) centered at 1028.25 nm is fiber-coupled to the waveguide by use of refractive-index-matching oil to avoid Fresnel reflection. The transmitted light is collected by an optical fiber and discriminated from residual room light by a monochromator, which is set to 1028.5 nm with a bandwidth wide enough to ensure detection of the resonance peak for all experimental situations, and detected by a photomultiplier tube [Fig. 1(b)]. This setup enabled measurement of the spectral response of the resonator for the temperature profiles produced along the waveguide [Fig. 1(c)], which result in thermally induced chirp profiles of the grating period.

This measurement technique results in a spectral convolution between the signal profile and the resonance profile under investigation. The FWHM of 40 MHz of the scanning narrow-linewidth laser is considered in order to de-convolute the measurement and obtain the correct line shape of the resonance, to which a Lorentzian curve is fitted to derive the FWHM linewidth.

## 3. Calculations and simulations

Our experimental investigations are complemented by theoretical considerations and simulations.

### 3.1 Resonance linewidth

The resonance linewidth results from the total losses of the resonator, which comprise the outcoupling losses, the intrinsic losses of the passive resonator, and the absorption losses introduced by the unpumped Yb ions. The outcoupling losses are due to the transmission of light through the distributed mirrors, where gratings 1 and 2 are defined as the part of the Bragg grating at the left- and right-hand side of the phase-shift center, respectively, and provide the reflectivity values  $R_1$  and  $R_2$ . If light penetrates into grating 1 and 2 by the penetration length  $\ell_{p1}$  and  $\ell_{p2}$ , respectively, resulting in the single-path resonator length

$$\ell_{res} = \ell_{p1} + \ell_{p2}, \quad (1)$$

its round-trip time becomes

$$t_{RT} = \frac{2\ell_{res}}{c}, \quad (2)$$

with  $c$  being the average speed of light in the waveguide medium (including the low- and high-index parts of each period and the thermally induced refractive-index change). These losses are quantified by the outcoupling decay-rate constant  $1/\tau_{out}$  according to



$$\frac{1}{\tau_{out}} = \frac{-\ln(R_1 R_2)}{t_{RT}}. \quad (3)$$

The intrinsic round-trip losses  $L_{RT}$ , a parameter commonly used in laser physics, of the passive resonator originate mostly in scattering at the corrugated Bragg mirrors and at the interfaces of the guiding medium, as well as scattering and absorption of light inside the guiding medium (but do not include the absorption or gain due to the Yb ions), i.e., these losses can alternatively be described by a propagation-loss coefficient per unit length,  $\alpha_{prop}$ :

$$L_{RT} = 1 - e^{-\alpha_{prop} 2\ell_{res}}. \quad (4)$$

Here the assumption has been made that the propagation losses do not change due to the adiabatic widening in the phase-shift region. These losses are quantified by the decay-rate constant  $1/\tau_{prop}$  according to

$$\frac{1}{\tau_{prop}} = \frac{-\ln(1 - L_{RT})}{t_{RT}} = c\alpha_{prop}. \quad (5)$$

The passive resonator is defined as the resonator at the transparency point, in which the atomic system provides neither absorption nor amplification of light. The decay-rate constant  $1/\tau_c$  of the passive resonator is the sum of the above-mentioned decay-rate constants. In the presence of additional absorption losses due to the unpumped atomic system with an absorption coefficient per unit length,  $\alpha_{abs}$ , resulting in the absorption decay-rate constant  $1/\tau_{abs}$  according to

$$\frac{1}{\tau_{abs}} = c\alpha_{abs}, \quad (6)$$

the total decay-rate constant  $1/\tau_L$  of photons inside the resonator then becomes

$$\frac{1}{\tau_L} = \frac{1}{\tau_{out}} + \frac{1}{\tau_{prop}} + \frac{1}{\tau_{abs}} = \frac{-\ln[R_1 R_2 (1 - L_{RT})]}{t_{RT}} + c\alpha_{abs} = \frac{-\ln[R_1 R_2]}{t_{RT}} + c(\alpha_{prop} + \alpha_{abs}). \quad (7)$$

The amplitude of the intracavity electric field decays exponentially with a lifetime of  $2\tau_L$ . Fourier transformation of such an exponential decay in the time domain to the frequency domain results in the electric-field amplitude per unit frequency interval, whose square represents the intensity spectral profile, which in case of insignificantly varying mirror reflectivities and photon decay time over the main part of the spectral resonance line results in an approximately Lorentzian-shaped spectral profile [34] with a FWHM linewidth given by

$$\Delta\nu_L = \frac{1}{2\pi\tau_L} = \frac{1}{2\pi} \left( \frac{1}{\tau_{out}} + \frac{1}{\tau_{prop}} + \frac{1}{\tau_{abs}} \right) = \Delta\nu_{out} + \Delta\nu_{prop} + \Delta\nu_{abs}, \quad (8)$$

where  $\Delta\nu_{out}$ ,  $\Delta\nu_{prop}$ , and  $\Delta\nu_{abs}$  are the resonance linewidths arising from the individual contributions to the total resonator losses. Although the spectral profiles are symmetric in the frequency domain [34], in this work we display the results in the wavelength domain, as the wavelength range over which the analysis is carried out is small enough to result in negligible asymmetry of the spectral profiles.

Although the temperature dependence of transition cross sections in laser systems can be significant [35,36], the absorption losses and the waveguide propagation losses remain approximately constant for the temperature range investigated here. A temperature increase results in a change of Bragg-grating period due to an increase in refractive index as well as thermal expansion of the device. These two effects together result in an increase in the optical path length that the light travels in each grating period. For the purpose of the simulations, we assume that the increase in refractive index is the dominating effect. For its temperature dependence, we make a first-order approximation,  $dn/dT = \text{const}$ . It results in a change of the

wavelength-dependent grating reflectivities and, consequently, the penetration lengths, the resonator length, and the outcoupling losses. A longitudinally non-uniform temperature increase further complicates the situation.

### 3.2 Simulations

We base our simulations of the spectral response of the DFB resonator on the characteristic-matrix approach, which is suitable to characterize light propagating through a stratified medium, as described by Born and Wolf [27] for a planar wave. The method consists in exploiting Maxwell's equations for the electric and magnetic field components in the dielectric medium under investigation and applying the appropriate boundary conditions between two adjacent media in the form of a matrix. For the case of a periodically stratified medium, such as a Bragg grating, one can define the characteristic matrix for one period as the multiplication of a matrix corresponding to a layer with lower refractive index (the etched part), namely  $M'_m$  by another matrix corresponding to a layer of higher refractive index (the non-etched part), namely  $M''_m$ , and thus obtain the matrix for period  $m$ , namely  $M_m = M'_m M''_m$ , given by

$$M_m = \begin{bmatrix} \cos \gamma'_m \cos \gamma''_m - \frac{p''_m}{p'_m} \sin \gamma'_m \sin \gamma''_m & -\frac{i}{p''_m} \cos \gamma'_m \sin \gamma''_m - \frac{i}{p'_m} \sin \gamma'_m \cos \gamma''_m \\ -ip''_m \cos \gamma'_m \sin \gamma''_m - ip'_m \sin \gamma'_m \cos \gamma''_m & \cos \gamma'_m \cos \gamma''_m - \frac{p'_m}{p''_m} \sin \gamma'_m \sin \gamma''_m \end{bmatrix}, \quad (9)$$

as defined in Born and Wolf. For the low-index layer of the  $m^{\text{th}}$  period (and for the high-index layer accordingly),  $\gamma'_m = \beta'_m \ell'_m$ , where  $\ell'_m$  is the length of the layer, the propagation constant  $\beta'_m$  is defined as usually,  $\beta'_m = k_0 p'_m$ , with  $p'_m = n'_m \cos \theta'_m$ , in which  $k_0$  is the wavenumber in vacuum,  $\theta'_m$  is the angle between the propagation vector and the direction of stratification (which corresponds to the waveguide axis for our device), and  $n'_m \cos \theta'_m$  is the effective refractive index, defined as a complex number in which the imaginary part corresponds to the continuous losses in the medium. The effective refractive index is obtained by use of a mode solver. The equation to be solved is a transcendental equation, known as the characteristic equation for our planar asymmetric waveguide, in which the parameters are the geometry of the waveguide and the refractive index profile. We consider TE polarization and a non-magnetic medium. In order to obtain the characteristic matrix for the entire structure, a multiplication of all the individual matrices  $M_m$  corresponding to the thermally chirped periods  $m$  is carried out. Our object of interest is the resonator, which is experimentally characterized by launching light and analyzing the outcoupled light, therefore, the first and last layers of the medium considered in the simulation are the refractive-index-matching oil, with  $n = 1.55$ .

This method is sometimes found in the literature as the transfer-matrix method (TMM) [37]. However, this terminology is not consistently used in the literature, might actually refer to very different approaches [38–40], and very often corresponds to the solutions of the coupled-mode theory (CMT) [5,41] in a matrix form. We chose the characteristic-matrix approach for its simplicity, for circumventing the requirement of knowing *a priori* the grating coupling strength (which would be required in CMT), for being valid for relatively large grating depth and refractive index difference, and, finally, for the absence of approximations other than the plane-wave approximation when describing the structures investigated in this work.

### 3.3 Thermal-chirp profile

A linear chirp profile of the Bragg-grating period  $\Pi(z)$  with position  $z$ ,



$$\Pi(z) = \Pi_0 [1 + \delta_{lin}(z - z_0)], \quad (10)$$

is considered to compare the simulation results of the spectral characteristics of the resonator with the experimental results. The simulations are then extended to quadratic and exponential chirp profiles.

For the simulation, we consider that the grating period along the  $z$  direction is the product of a constant physical length multiplied by the refractive index profile along  $z$ , in which we impose the desired chirp profile [Fig. 1(d)]. In Eq. (10), the chirp coefficient  $\delta_{lin}$  has the dimension ( $\text{m}^{-1}$ ), i.e., it represents the chirp per unit length. The Bragg mirrors of the DFB resonator are constituted by a sequence of adjacent layers of high and low refractive indices, the latter being achieved by partially etching the cladding layer of the waveguide. Figure 1(d) depicts the effective refractive index along the waveguide of both types of layers, when a linear chirp profile is considered. The constant value at positions  $z \leq z_0 = 2.5$  mm is obtained by use of a mode solver (software COMSOL), for both the etched and non-etched layers (using the. For  $z > z_0$ , the initial effective refractive index at the position  $z_0 = 2.5$  mm increases linearly with length  $z$  according to the value of the linear chirp coefficient  $\delta_{lin}$ . The additional increase of effective refractive index in the phase-shift region, as a result of the tapering of the waveguide width according to the  $\sin^2$  function centered at position  $z = 7$  mm, is also calculated [Fig. 1(d)].

#### 4. Results and discussion

Firstly, we characterize the spectral response of the DFB resonator as a function of temperature without thermal chirp and derive the relevant parameters that will allow us to investigate and understand the situation with thermal chirp.

##### 4.1 Spectral response without thermal chirp

The calculated reflectivity curves of gratings 1 and 2 and the wavelength of the resonance peak for different sample temperatures are displayed in Figs. 2(a) and 2(b), respectively. In a first-order Bragg grating, the period  $\Lambda = \lambda_B / (2n_{eff})$ , the Bragg wavelength  $\lambda_B$ , the grating reflectivities, and the resonance wavelength shift in the same way with temperature. Consequently, the reflectivities at the resonance wavelength and, therefore, also the linewidth remain the same. By homogeneously heating the entire sample, we determine experimentally the temperature dependence of spectral response of the DFB resonator [Fig. 2(c)]. The dependence of wavelength shift of the resonance peak with temperature [Fig. 2(d)] is approximately linear and amounts to 12.0 pm/K for ~1028 nm, i.e., a relative wavelength shift of  $\sim 1.2 \times 10^{-5} \text{ K}^{-1}$ , which is in reasonable agreement with the values of  $19 \pm 1$  pm/K [10] and 20 pm/K [42] reported for ~1560–1590 nm, therefore corresponding to the same relative wavelength shift. From the shift of peak wavelength with temperature, we derive the value of  $dn/dT = 1.86 \times 10^{-5} \text{ K}^{-1}$ . Since part of the shift is due to sample expansion, this value represents an upper limit to the refractive index change with temperature. The value is higher than the corresponding value of  $0.83 \times 10^{-5} \text{ K}^{-1}$  in  $\text{Y}_3\text{Al}_5\text{O}_{12}$  and the absolute of the two values of  $-0.43 \times 10^{-5} \text{ K}^{-1}$  and  $-0.20 \times 10^{-5} \text{ K}^{-1}$  for the  $c$ - and  $a$ -axes, respectively, in  $\text{YLiF}_4$  (see Ref [43]. and Refs. therein), but smaller than the value of  $4.58 \times 10^{-5} \text{ K}^{-1}$  previously reported for amorphous  $\text{Al}_2\text{O}_3$  [44]. In Fig. 2(c), the measured line shape of the device exhibits a small asymmetry, which is likely due to the measurement method, but its exact origin is unclear. The change of FWHM linewidth of the resonance with temperature is displayed in Fig. 2(e), indicating that the linewidth remains unchanged within the experimental errors. This is because the resonator losses, particularly the outcoupling losses at the resonance wavelength, do not change significantly when homogeneously heating the sample.

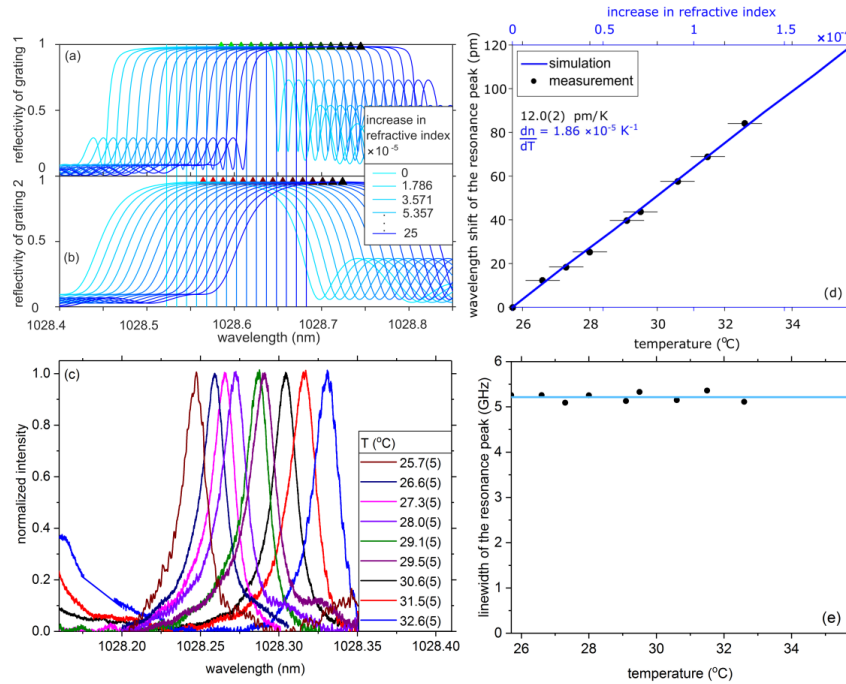


Fig. 2. Results when homogeneously heating the sample to different temperatures. Simulated reflectivity of (a) grating 1 and (b) grating 2 as a function of wavelength. Vertical lines: wavelength of resonance peak at each temperature; green and red triangles: maximum reflectivity of grating 1 and grating 2, respectively. Lightest (darkest) color: sample at room (highest) temperature. (c) Measured spectral response of DFB resonator. (d) Measured (dots) and simulated (line) wavelength shift of resonance peak as a function of temperature and according increase in refractive index. (e) Measured (dots) FWHM linewidth of resonance peak as a function of temperature. The average value (line) is  $5.26 \pm 0.10$  GHz.

#### 4.2 Spectral response with thermal chirp: simulation

In Fig. 3 we present the simulated spectral response of the resonator with a linear chirp profile. The reflectivity profile of (a) grating 1 and (b) grating 2 is displayed for the different values of linear chirp coefficient  $\delta_{lin}$ , which ranges from 0 to  $6.5 \times 10^{-2} \text{ m}^{-1}$  in steps of  $\sim 2.241 \times 10^{-3} \text{ m}^{-1}$ . The vertical lines indicate the wavelength of the resonance peak resulting from the combined effect of the two grating profiles, whereas the triangles indicate the wavelength where the maximum reflectivity of each of the two gratings occurs. Their dependencies on linear chirp coefficient  $\delta_{lin}$  are shown separately in Fig. 3(c).

We obtain the reflectivity spectra of both gratings and the resulting Lorentzian-shaped resonance from the same simulation, enabling us to place the resonance within the reflection band of the gratings, as depicted in Figs. 3(a) and 3(b). We set the continuous losses equal to zero to correctly simulate the reflectivity spectra of gratings 1 [Fig. 3(a)] and 2 [Fig. 3(b)]. The transmission spectrum is obtained by considering also the absorption and propagation losses [Fig. 3(e)]. The dependence of the wavelength of the resonance peak on the chirp profile is the same, independent of the value of the continuous losses. We have not experimentally investigated the reflectivity spectrum of each grating individually, which would require cutting the sample into two at the phase-shift center, to confirm if the simulation and experimental results agree in this regard.

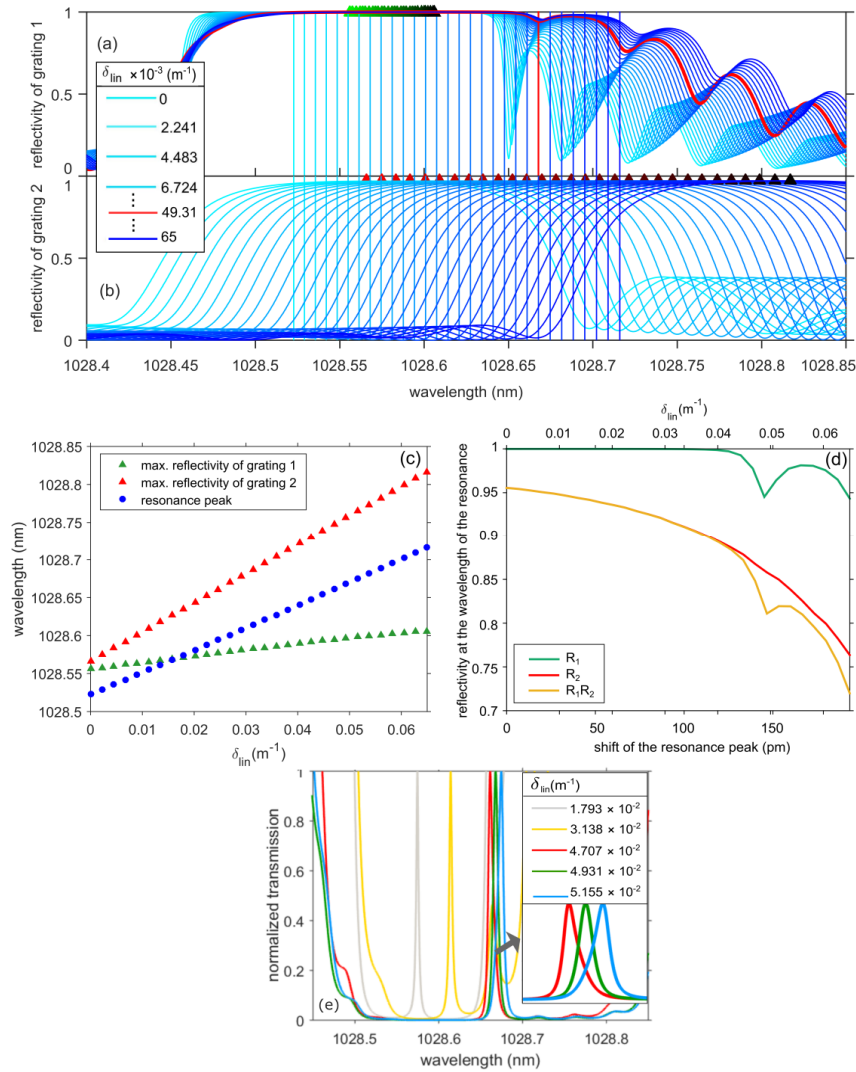


Fig. 3. Simulated results with chirped grating. Reflectivity of (a) grating 1 and (b) grating 2 as a function of wavelength. The curves in red are for the case  $\delta_{lin} = 0.0493$ , discussed in detail in the text. Vertical lines: wavelength of resonance peak at each temperature profile; green and red triangles: maximum reflectivity of grating 1 and grating 2, respectively. Lightest (darkest) color: sample without (highest) chirp. (c) Dependence of the wavelengths of resonance peak (blue circles) and maximum reflectivity of grating 1 (green triangles) and grating 2 (red triangles) on  $\delta_{lin}$ . (d) Reflectivity  $R_1$  and  $R_2$  at the wavelength of the resonance peak provided by gratings 1 and 2, respectively, and their product  $R_1 R_2$  as a function of the shift of wavelength of the resonance peak (lower x-axis) resulting from the linear chirp coefficient (upper x-axis). (e) Transmission spectrum of the resonator as a function of wavelength, shown for five different values of  $\delta_{lin}$  as indicated in the legend. The intensity is normalized to unity at each resonance peak. Inset: resonant peaks located at the left-hand side of, coincident with, and at the right-hand side of the reflectivity dip provided by grating 1.

From Fig. 3(c), we identify that the wavelength of the resonance peak (blue circles) shifts linearly towards larger values for increasing values of  $\delta_{lin}$ , which is a consequence of the linear increase in the accumulated phase shift. By identifying, for each  $\delta_{lin}$ , the wavelength of the resonance peak and the reflectivity provided by gratings 1 and 2 at this specific wavelength, namely  $R_1$  and  $R_2$ , we determine how the reflectivity values change for increasing values of  $\delta_{lin}$  [Fig. 3(d)].

The range over which the spectral response of grating 1 shifts is smaller than the range over which the resonance shifts, because the sections of the structure that belong to this grating are subject to a smaller deviation from the initial period [Fig. 1(d)]. As a consequence, the resonance peak experiences a dip in the reflectivity spectrum provided by grating 1, as highlighted in red in the curves in Fig. 3(a) for  $\delta_{lin} = 0.0493 \text{ m}^{-1}$ . This dip is the spectral feature observed in Fig. 3(a) at wavelengths around 1028.655 nm for values of  $\delta_{lin}$  around  $0.05 \text{ m}^{-1}$ , as can also be observed in Fig. 3(d). On the other hand, the reflectivity spectrum of grating 2 shifts over a larger range than the resonance [Fig. 3(b)], because in this part of the sample the deviation from the initial period is large [Fig. 3(d)], and the reflectivity values  $R_2$  provided by this grating decrease monotonically as  $\delta_{lin}$  increases [Fig. 3(d)].

Figure 3(e) shows the normalized transmission of the resonator for five different values of  $\delta_{lin}$ . When comparing Figs. 3(a) and 3(b) with Fig. 3(e), we note that the resonance peak is broad enough to experience non-constant reflectivity values, particularly in those wavelength regions where the reflectivity values vary considerably as a function of wavelength. The result of this wavelength-dependent reflectivity is an asymmetric, non-Lorentzian-shaped peak [34], as can be observed in the inset of Fig. 3(e). The inset also displays the consequence of the dip in the reflectivity spectrum provided by grating 1:  $\delta_{lin} = 4.707 \times 10^{-2} \text{ m}^{-1}$  (red curve),  $4.931 \times 10^{-2} \text{ m}^{-1}$  (green curve), and  $5.155 \times 10^{-2} \text{ m}^{-1}$  (blue curve) result in resonance peaks located at the left-hand side, at the center of, and at the right-hand side of the reflectivity dip, respectively. The red and blue curves are rather asymmetric; leading to larger FWHM values in the simulation [see later in Fig. 4(c)].

The reflection band changes drastically when the chirped profiles are imposed on the grating. This is a result of the change in the individual spectral responses provided by gratings 1 and 2, as is confirmed by Figs. 3(a) and 3(b). In addition to their entire spectral responses shifting towards longer wavelength, notably the reflection provided by grating 1 for longer wavelengths presents a smoother and broader profile, therefore resulting in a broader and distorted reflection band, as observed in Fig. 3(e).

#### 4.3 Spectral response with thermal chirp: experiment and comparison with simulation

The spectral profile of the resonance is obtained experimentally with the setup shown in Fig. 1(b) for the temperature profiles produced as shown in Fig. 1(c). The resonance peak and part of the adjacent features of the resonator transmission spectrum are displayed in Fig. 4(a). Each resonance peak was fitted by a Lorentzian function and both were simultaneously normalized such that the peak value of the Lorentzian function is unity.

The simulation results indicate that the wavelength of the resonance peak [Fig. 4(b)] is mostly a result of the grating-period value at the phase-shift center, whereas the additional wavelength shift resulting from the grating chirp is small. For example, a wavelength shift of the resonance peak of more than 140 pm comprised only 5 pm of shift due to the grating chirp. This was verified by simulating the spectral response of a grating with a linear chirp profile and the constraint that its period at the phase-shift center was always the same. Since the increase in grating period at the phase-shift center is proportional to  $\delta_{lin}$ , the shift of wavelength of the resonance peak is a linear function of  $\delta_{lin}$  [solid line in Fig. 4(b)]. The measured values of wavelength of the resonance peak also exhibit a linear dependence on the estimated temperature at the phase-shift center [dots in Fig. 4(b)], suggesting that the first-order approximation of the temperature profile in Fig. 1(c) and of  $dn/dT$  is reasonable.

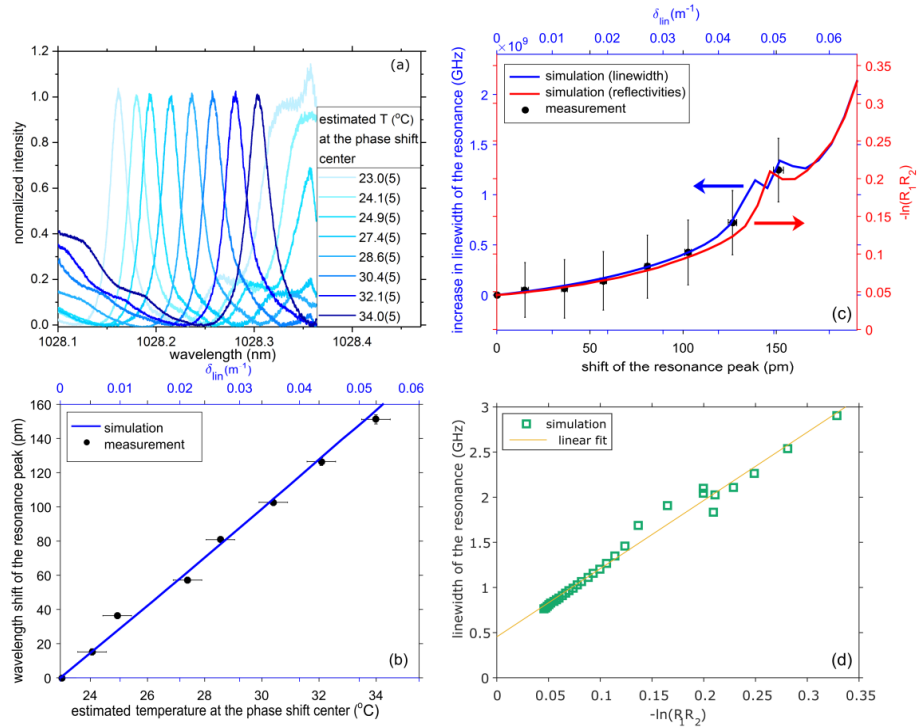


Fig. 4. Measured results with thermally chirped grating and comparison with simulations. (a) Measured resonances for the thermally induced chirp profiles. (b) Wavelength shift of the resonance peak: experimental results (dots) as a function of estimated temperature at phase-shift center (bottom x-axis); simulation results (line) as a function of linear chirp coefficient (top x-axis). (c) Experimental (dots) and simulated (lines) increase in linewidth of the resonance as a function of wavelength shift of the resonance peak. Blue curve: linewidth of the resonance calculated with the characteristic-matrix approach; red curve: simulation exploiting the reflectivity values of Fig. 4(d) in Eq. (3) for  $-\ln(R_1 R_2)$ . (d) Relation between linewidth and the parameter  $-\ln(R_1 R_2)$  (green squares). From the linear fit (yellow curve) the single-path resonator length  $\ell_{res}$  is calculated.

The wavelength shift induced by the increasing temperature at the phase-shift center [Fig. 4(b)] is 13.9 pm/K, which is slightly larger than the value of 12.0 pm/K derived when heating the sample homogeneously [Fig. 1(b)]. This difference is probably due to the inaccuracy in determining the temperature exactly at the phase-shift center, and an error in sample position as small as 0.5 mm would explain this discrepancy.

After cleaning and annealing of the sample, linewidth measurements were consistently repeated six times over a span of several days, during which we observed that the longer the sample had stayed in contact with the thermally conductive material [Fig. 1(b)], the larger was the resonance linewidth of the resonator without chirp, whereas the additional increase in linewidth with the thermally imposed chirp profiles remained the same. This is a result of increased propagation losses due to moisture absorption by the sample when in long-term direct contact with the thermally conductive material, consisting of thermal paste. The experimental linewidth values [Fig. 4(c)] are the average of the six measurements, with the error bars corresponding to the standard deviation in each data set, whereas Fig. 4(a) displays the first of these six measurements. In the simulations, we assume constant propagation losses of  $\alpha_{prop} = 0.2$  dB/cm, which do not take this loss deterioration over time into account. Therefore, the linewidth values obtained experimentally (averaged over the six measurements) are larger than the values obtained in the simulations. The absorption losses



are  $\alpha_{abs} = 0.33$  dB/cm [45], resulting in a sum of propagation and absorption losses of  $\alpha_{prop} + \alpha_{abs} = 0.53$  dB/cm assumed in the simulation.

In Fig. 4(c), the measured increase in resonance linewidth (dots) as a function of wavelength shift of the resonance peak and the simulation results (lines) as functions of linear chirp coefficient are depicted. The blue curve displays the linewidth increase simulated from the spectral response of the resonator by use of the characteristic-matrix approach. The two peaks at a wavelength shift of around 150 pm are a consequence of the resonance peak crossing the dip in the reflectivity spectrum of grating 1, resulting in the line shape asymmetry displayed in the inset of Fig. 3(e). For the experimental spectra in Fig. 4(a), the resonance peaks corresponding to  $T = 28.6^\circ\text{C}$ ,  $30.4^\circ\text{C}$ , and  $32.1^\circ\text{C}$  present a certain asymmetry, which could be for the same reason.

The red curve in Fig. 4(c) shows the calculation of  $-\ln(R_1R_2)$ , with the values of  $R_1R_2$  taken from Fig. 3(d). Comparison of the two simulation results (blue and red lines) shows that the general increase in linewidth is very similar, indicating that the decrease in  $R_1$  and  $R_2$  is largely responsible for the increase in resonance linewidth, which is consistent with Eqs. (8) and (10), because the propagation and absorption losses remain constant when increasing the chirp during each of the six measurements. However, the two curves are not in agreement in the region where the wavelength shift is  $\sim 150$  pm, because the red curve is calculated by use of the values of  $R_1R_2$  exactly at the wavelength of the resonance peak, thereby ignoring the wavelength-dependent grating reflectivity, resulting in the asymmetry of the Lorentzian-shaped resonance [inset in Fig. 3(e)]. The peak in the red curve corresponds to  $\delta_{lin}$  at the point where  $R_1$  is minimum, as expected from the analytical expressions of Eqs. (3) and (8). In order to completely explain the spectral response of the resonator, one has to consider the wavelength-dependent reflectivity provided by the gratings, which depends on the linear chirp coefficient.

According to Eq. (8), the resonance linewidth is due to the outcoupling, propagation, and absorption losses. Imposing a chirp in the grating period changes the refractive index  $n$ , the resonator length  $\ell_{res}$  of Eq. (1) and, consequently, the round-trip time  $t_{RT}$  of Eq. (2). All three losses depend on  $c$  and, therefore,  $n$ . However, the change in refractive index is small, reaching a maximum of 0.00025, hence its effect is negligible. The parameters  $\alpha_{prop}$  and  $\alpha_{abs}$  are defined per unit length, hence are independent of  $\ell_{res}$ . Moreover, for a temperature increase of a few degrees,  $\alpha_{prop}$  and  $\alpha_{abs}$  remain approximately constant, as confirmed by the result of Fig. 2(e). Consequently, the change in  $\Delta\nu_{prop}$  and  $\Delta\nu_{abs}$  is negligible. In contrast, from Fig. 3(d) it is evident that  $R_1$  and  $R_2$  change significantly with a few degrees of temperature change, causing the linewidth to increase.

The linewidth  $\Delta\nu_L$  of the resonance as a function of grating reflectivities,  $-\ln(R_1R_2)$ , is displayed in Fig. 4(d). The relationship is approximately linear, as indicated by the linear fit. For chirp values in the region where  $R_1$  exhibits the dip, the value of  $R_1$  changes rapidly forth and back, hence in the representation of Fig. 4(d), for  $-\ln(R_1R_2) \approx 0.14$ , there are two linewidth values. Each corresponds to a distinct chirp value and to a different asymmetric Lorentzian-shaped resonance.

To calculate the outcoupling losses from Eqs. (8) and (3) requires knowledge of the resonator length  $\ell_{res}$ , however, there is no unique definition of the penetration length into a Bragg grating in the literature. In Eq. (8),  $\Delta\nu_L = \Delta\nu_{out} + C_1 = -\ln(R_1R_2)/(2\pi t_{RT}) + C_1$ , where  $C_1$  stands for the constant contributions from the propagation and absorption losses. This can only lead to a linear relationship, if we assume that  $1/(2\pi t_{RT}) = C_2$  is constant, hence  $\Delta\nu_L = -\ln(R_1R_2)C_2 + C_1$ . From this linear fit, we derive  $C_1 = 0.453$  GHz and  $C_2 = 7.56$  GHz. By use of Eqs. (5) and (6), from the parameter  $C_1$  we obtain  $\alpha_{prop} + \alpha_{abs} = 0.66$  dB/cm. As discussed previously, in regions where the resonance experiences a strongly wavelength-dependent reflectivity, the asymmetrically Lorentzian-shaped resonances have a larger linewidth than what is calculated analytically. Since the linear fit shown in Fig. 4(d) is influenced by the resonances that experience this situation, the parameters  $C_1$  and  $C_2$  assume slightly larger



values than those we would expect, therefore, from the value of  $C_1$  we derive a larger value for  $\alpha_{prop} + \alpha_{abs}$  than we entered into the simulation. Finally, exploiting Eq. (2) and the parameter  $C_2$ , we derive a single-path resonator length of  $\ell_{res} = 1.55$  mm, which represents the penetration length into gratings 1 and 2. Since this value was calculated using all considered chirp profiles, it corresponds to an average  $\ell_{res}$ , and further investigation would be required in order to understand the effect of the chirp on  $\ell_{res}$ , but the linear relationship proposes that the change in  $\ell_{res}$  is rather small.

We performed the same simulation analysis for quadratic and exponential chirp profiles. The trend in the linewidth increase is consistent with that induced by the linear chirp, indicating that the understanding of the linewidth being the direct consequence of the resonator losses can be generalized and extended to virtually any grating profile, provided that the reflectivity at the wavelength of the resonance peak, resulting from the grating chirp profile, is determined. The less significantly the grating reflectivities and consequent photon-decay time vary over the main part of the spectral resonance line, the better is the agreement between the linewidth increase obtained via the spectral response of the resonator and via the increase in outcoupling losses.

## 5. Conclusion

We have investigated the spectral response of a DFB rib waveguide resonator experimentally and by simulations using the characteristic-matrix approach. The resonator was subject to thermal effects, namely a (i) uniform heating of the entire sample or (ii) a close-to-linear temperature gradient along the waveguide. For uniform heating of the sample, we measured an approximately linear dependence of wavelength shift of the resonance peak on temperature of 12.0 pm/K at  $\sim 1028.5$  nm, equivalent to a relative wavelength shift of  $\sim 1.2 \times 10^{-5} \text{ K}^{-1}$ , whereas the FWHM linewidth of the Lorentzian-shaped resonance remained unchanged. This is a consequence of an increase in the accumulated phase shift, whereas the total resonator losses remained constant. When a linear chirp profile was produced in the grating period, the wavelength of the resonance peak again presented a linear dependence on the estimated temperature at the phase-shift center (from the experiments) and on the linear chirp coefficient  $\delta_{lin}$  (from the simulations), but the FWHM linewidth increased.

The outcoupling, propagation, and absorption losses are the parameters responsible for the FWHM linewidth of the resonance. Whereas only the first changes when a chirp profile is imposed on the grating, it is of crucial importance to understand how the reflectivity spectrum provided by the gratings is experienced by the resonance peak. A chirp profile leads to distortions of the reflectivity spectrum provided by the gratings, and when the resonance peak is broad enough to experience non-constant reflectivity values, the result is an asymmetric, non-Lorentzian-shaped peak and, therefore, the FWHM linewidth cannot be analytically calculated. For situations where this effect is negligible, we have demonstrated that the increase in the outcoupling losses is largely responsible for the increase in the FWHM linewidth of the resonance. In simulations for a quadratic and exponential chirp profiles, we have generalized this statement, and verified that the effect is independent on the chirp profile.

This work is especially valuable on the scope of the design and control of resonators with distributed mirrors, subject to thermal effects, where precise control of the wavelength and line shape of the emission is required.

## Funding

European Research Council (ERC) Advanced Grant “Optical Ultra-Sensor” No. 341206.